

Preclinical Evaluation of ^{18}F -RO6958948, ^{11}C -RO6931643, and ^{11}C -RO6924963 as Novel PET Radiotracers for Imaging Tau Aggregates in Alzheimer Disease

Michael Honer¹, Luca Gobbi¹, Henner Knust¹, Hiroto Kuwabara^{2,3}, Dieter Muri¹, Matthias Koerner¹, Heather Valentine^{2,3}, Robert F. Dannals², Dean F. Wong²⁻⁶, and Edilio Borroni¹

¹Roche Pharma Research and Early Development, Roche Innovation Center Basel, F. Hoffmann-La Roche Ltd., Basel, Switzerland;

²PET Center, Division of Nuclear Medicine, Russell H. Morgan Department of Radiology, Johns Hopkins University School of Medicine, Baltimore, Maryland; ³Section of High Resolution Brain PET, PET Center, Division of Nuclear Medicine, Russell H. Morgan Department of Radiology, Johns Hopkins University School of Medicine, Baltimore, Maryland; ⁴Solomon H. Snyder

Department of Neuroscience, Johns Hopkins University School of Medicine, Baltimore, Maryland; ⁵Department of Psychiatry and Behavioral Sciences, Johns Hopkins University School of Medicine, Baltimore, Maryland; and ⁶Department of Neurology, Johns Hopkins University School of Medicine, Baltimore, Maryland

Tau aggregates and amyloid- β (A β) plaques are key histopathologic features in Alzheimer disease (AD) and are considered targets for therapeutic intervention as well as biomarkers for diagnostic in vivo imaging agents. This article describes the preclinical in vitro and in vivo characterization of 3 novel compounds—RO6958948, RO6931643, and RO6924963—that bind specifically to tau aggregates and have the potential to become PET tracers for future human use. **Methods:** RO6958948, RO6931643, and RO6924963 were identified as high-affinity competitors at the ^3H -T808 binding site on native tau aggregates in human late-stage AD brain tissue. Binding of tritiated compounds to brain tissue sections of AD patients and healthy controls was analyzed by macro- and microautoradiography and by costaining of tau aggregates and A β plaques on the same tissue section using specific antibodies. All 3 tracer candidates were radiolabeled with a PET nuclide and tested in vivo in tau-naïve baboons to assess brain uptake, distribution, clearance, and metabolism. **Results:** ^3H -RO6958948, ^3H -RO6931643, and ^3H -RO6924963 bound with high affinity and specificity to tau aggregates, clearly lacking affinity for concomitant A β plaques in human AD Braak V tissue sections. The specificity of all 3 radioligands for tau aggregates was supported, first, by binding patterns in AD sections comparable to the tau-specific radioligand ^3H -T808; second, by very low nonspecific binding in brain tissue devoid of tau pathology, excluding significant radioligand binding to any other central nervous system target; and third, by macroscopic and microscopic colocalization and quantitative correlation of radioligand binding and tau antibody staining on the same tissue section. RO6958948, RO6931643, and RO6924963 were successfully radiolabeled with a PET nuclide at high specific activity, radiochemical purity, and yield. After intravenous administration of ^{18}F -RO6958948, ^{11}C -RO6931643, and ^{11}C -RO6924963 to baboons, PET scans indicated good brain entry, rapid washout, and a favorable metabolism pattern. **Conclusion:** ^{18}F -RO6958948, ^{11}C -RO6931643, and ^{11}C -RO6924963 are promising PET tracers for visualization of tau aggregates in AD.

Head-to-head comparison and validation of these tracer candidates in AD patients and healthy controls will be reported in due course.

Key Words: autoradiography; tauopathy; neurology; PET; tau; Alzheimer disease

J Nucl Med 2018; 59:675–681

DOI: 10.2967/jnumed.117.196741

Tau is a microtubule-associated protein that exists in multiple isoforms and posttranslational modifications. The protein becomes hyperphosphorylated and aggregates to neurofibrillary tangles (NFTs) and neuropil threads in the brains of Alzheimer disease (AD) patients. Histologic analyses of brains from AD autopsy cases have suggested that the spread and density of NFTs correlate with the cognitive status of patients (1,2). Noninvasive methods to detect these abnormal proteins are therefore highly desirable for early and accurate diagnosis of the disease and to support therapeutic advances in managing tau-directed therapies.

Several PET tracers characterized in vitro in NFT-rich AD brain tissue and in vivo in AD patients have recently been reported and reviewed in the literature (3–5). ^{18}F -flortaucipir (also known as ^{18}F -AV-1451 or ^{18}F -T807) was the first published PET tracer to show promise for visualizing and quantifying NFT pathology in AD patients (6) and is currently the most widely studied tau PET tracer. This tracer has limitations: it does not reach a steady state during a typical imaging duration, making quantification challenging (7,8), and it shows some high-affinity off-target binding (9,10). ^{11}C -PBB3 has been shown to provide a specific signal in AD patients that is differentiated from the binding pattern of amyloid- β (A β) plaque PET tracers, but brain uptake of the tracer was minimal (11). Multiple ^{18}F -labeled NFT PET tracers have been evaluated by investigators at Tohoku University, the most recent being ^{18}F -THK5351, which has shown high-affinity binding to monoamine oxidase (MAO)-B (12). Merck recently presented the preclinical characterization of the NFT PET tracer ^{18}F -MK-6240 (13,14). ^{18}F -MK-6240 has high affinity for NFT-rich AD brain homogenates, and self-blocking studies in rhesus monkeys did not reveal

Received Jun. 6, 2017; revision accepted Jul. 25, 2017.

For correspondence or reprints contact: Michael Honer, Pharma Research and Early Development (pRED), Roche Innovation Center Basel, F. Hoffmann-La Roche Ltd., 4070 Basel, Switzerland.

E-mail: michael.honer@roche.com

Published online Sep. 28, 2017.

COPYRIGHT © 2018 by the Society of Nuclear Medicine and Molecular Imaging.

any displaceable tracer binding. ^{18}F -JNJ64349311, another promising tau PET tracer candidate with favorable preclinical characteristics, was recently described by Janssen (15).

Our goal was to develop a novel tau PET tracer with excellent selectivity, sensitivity, and pharmacokinetic properties for the purpose of detecting longitudinal changes in the distribution and density of tau load in therapeutic intervention trials on AD patients. To this end, 3 potential tau PET tracer candidates—RO6958948 (2-(6-fluoro-pyridin-3-yl)-9*H*-dipyrido[2,3-*b*:3',4'-*d*]pyrrole), RO6931643 (*N*-methyl-2-(3-methylphenyl)imidazo[1,2-*a*]pyrimidin-7-amine), and RO6924963 (2-(4-methoxyphenyl)imidazo[1,2-*a*]pyrimidin-7-amine)—were developed for eventual head-to-head comparison in the same AD patient population. In this article, we report the *in vitro* and *in vivo* preclinical characterization of these 3 tracer candidates as PET imaging agents for tau aggregates.

MATERIALS AND METHODS

General

All chemicals, unless otherwise stated, were purchased from commercial suppliers and used without further purification. RO6958948, RO6931643, RO6924963, and T808 were tritiated at Roche. ^3H -RO6958948 and ^3H -RO6924963 were prepared by hydrogen tritium exchange in the presence of an iridium catalyst; ^3H -RO6931643, by ^3H -methylation of a des-methyl precursor. All tritiated ligands were obtained with a specific activity of more than 900 GBq/mmol.

^{11}C and ^{18}F radiolabeling was performed at the Johns Hopkins University PET Center, as described elsewhere (16,17). The radiochemical identity of tracer candidates was confirmed by coinjection of the authentic reference standard with the radiotracer. Specific activity and radiochemical purity were determined by high-performance liquid chromatography. The calculated specific activity of the PET radiotracers at the end of synthesis was over 500 GBq/ μmol , with a radiochemical purity of more than 96%.

Tissues and Animals

Fresh-frozen human brain tissue blocks were purchased from the Banner Sun Health Research Institute and Lund University. Pathologic diagnosis was made according to standard National Institute on Aging-Reagan Institute criteria based on neuropathologic data. Male baboons (*Papio anubis*) were used for the PET experiments and were kept fasting for 12 h before each PET study. The experimental protocol was approved by the Animal Care and Use Committee of Johns Hopkins University.

In Vitro Autoradiography

Tissue sections (10 μm thick) from fresh-frozen human brain were incubated for 60 min in Ringer buffer containing the radioligand at

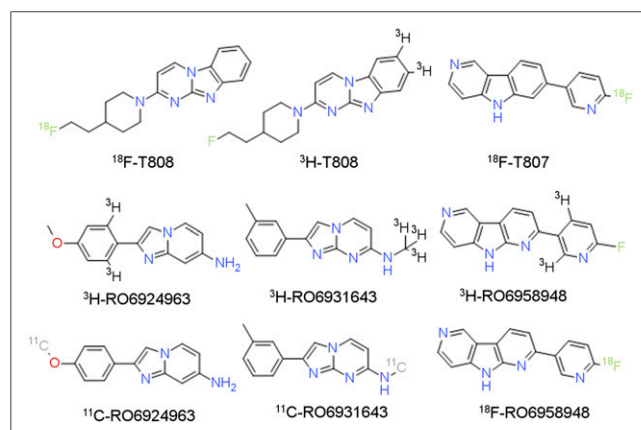


FIGURE 1. Structures of NFT ligands.

TABLE 1
Affinities and Details About Specific Binding and Nonspecific Binding in Autoradiography

Parameter	RO6958948	RO6931643	RO6924963
Affinity (IC_{50} in nM)	18.5	10.0	5.5
Gray matter-to-white matter ratio in AD Braak V	8	5	11
Specific binding in gray matter (fmol/mg of protein)	5,162	5,320	10,250

IC_{50} = half-maximal inhibitory concentration.

room temperature. For affinity testing, 10 nM ^3H -T808 was coincubated with 10 nM unlabeled candidate compound. For macroautoradiographic analysis, the tritiated compound was incubated at 3 nM. For microautoradiography, a radioligand concentration of 30 nM was used. After incubation, all sections were rinsed 3 times for 5 min in Tris buffer and dipped 3 times in distilled water at 4°C . Slide-mounted brain sections were dried for at least 3 h and exposed to a BAS-TR 2025 imaging plate (Fuji) with a ^3H -microscale (RPA-510; GE Healthcare) for 5 d. The imaging plate was scanned with 25- μm resolution in a high-resolution plate scanner (BAS-5000). For microautoradiography, the sections were dipped in NTB emulsion (Kodak) and kept for more than 2 wk at 4°C in a dark box before being developed for 2 min in Kodak developer solution, fixed for 5 min in Kodak fixer solution and finally analyzed under the light microscope. Visualization and quantification of the macroautoradiograms were performed with the MCID image analysis program (Imaging Research Inc.). The total amount of radioligand bound to the brain areas of interest was expressed as femtomoles of bound radioligand per milligram of protein. For affinity testing of unlabeled tracer candidates, total binding was determined in gray matter regions of late-stage AD tissue sections with high tau pathology, nonspecific binding was determined in a tau-free white matter region of the same tissue section, and specific binding was calculated as follows: specific binding = total binding – nonspecific binding. The displacement potency of novel unlabeled test compounds was calculated according to the following formula: $100 - (\text{specific binding, test compound} / \text{specific binding, radioligand only}) \times 100\%$. For quantitative assessment of novel tritiated compounds, nonspecific binding was determined by calculating radioligand binding in gray matter regions of healthy control tissue sections devoid of tau pathology. Specific binding to tau aggregates was assessed by quantifying the difference in binding to tau-rich cortical gray matter in AD tissue versus cortical gray matter of healthy controls. Signal-to-noise ratios were quantified by calculating gray matter-to-white matter ratios of radioligand binding to late-stage AD cortical tissue sections.

Immunohistochemistry

Macro- and microautoradiograms were analyzed by costaining of tau aggregates and A β plaques on the same tissue section. For staining of tau aggregates, either AT8 (Thermo Scientific) or pS422 (generated in-house) was used, and for staining of A β plaques, the monoclonal antibody (mAb) BAP-2a (generated in-house) was used. The sections were fixed for 3 min in 100% acetone at -20°C . Blockade was done for 20 min in blocking buffer (1 \times phosphate-buffered saline, 1% natural goat serum, ovalbumin, and bovine serum albumin). After antibody incubation (5–10 $\mu\text{g/mL}$, 2 h at room temperature) and 4',6-diamidino-2-phenylindole staining, the sections were washed 3 times for 5 min in 1 \times phosphate-buffered saline before being incubated with 0.3% Sudan Black

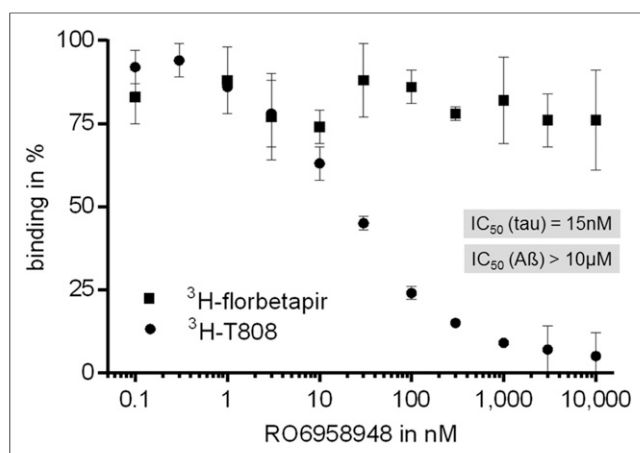


FIGURE 2. Displacement of ^3H -T808 or ^3H -florbetapir binding to AD tissue sections by increasing concentrations of RO6958948. IC_{50} = half-maximal inhibitory concentration.

for reduction of autofluorescence. The stained sections were scanned with the Metafer4 automated scanning system (MetaSystems) or the Pano-ramic 250 Flash digital slide scanner (3DHitech).

PET Imaging

Six baboons ranging in weight from 22 to 28 kg were used for this study. Each animal was positioned in an ECAT HRRT brain PET scanner (Siemens). A 6-min transmission scan with a 37-MBq ^{137}Cs point source was initially obtained for attenuation correction. The following ranges of radiochemical and mass doses were used for the PET studies: 417–780 MBq and 0.04–26 μg . Ninety-minute dynamic PET scanning in 3-dimensional list mode started immediately on initiation of tracer injection. PET data were reconstructed, correcting for attenuation, scatter, and dead time (18), into four 15-s, four 0.5-min, three 1-min, two 2-min, five 4-min, and twelve 5-min frames. The final spatial resolution was expected to be about 2.3 mm in full width at half maximum in 3 directions. Arterial blood was sampled every 5 s during the first 2 min of the scan and thereafter at intervals of progressively increasing duration. The blood samples were immediately centrifuged, and the plasma samples were counted for radioactivity using a γ -counter that was cross-calibrated daily against the ECAT HRRT scanner. Plasma samples taken at 5, 10, 20, 30, 60, and 90 min after tracer injection were analyzed by high-performance liquid chromatography for the presence of each parent compound and its radio-labeled metabolites. Time-activity curves for the parent compound were obtained by applying interpolated parent fractions of high-

performance liquid chromatography samples to the total time-activity curves. The metabolite-corrected plasma time-activity curves were used as the input function for tissue tracer kinetic modeling. Volumes of interest previously defined on structural MRIs of individual animals included the frontal, temporal, parietal, and occipital cortices and the cerebellum, putamen, and thalamus. The kinetics of the radioligands were evaluated with standard 1- and 2-tissue compartmental models and the plasma reference graphical analysis (19).

RESULTS

RO6958948, RO6931643, and RO6924963 were identified through a PET tracer discovery and optimization program. T807 and T808 served as seed structures for the synthesis of approximately 550 novel derivatives. The 3 compounds were identified as high-affinity displacers at the ^3H -T808 binding site in NFT-rich AD Braak V/VI cortical tissue sections. T808 is a selective, high-affinity NFT ligand with excellent in vitro properties (Fig. 1) (20). The half-maximal inhibitory concentrations for RO6958948, RO6931643, and RO6924963 were 18.5, 10.0, and 5.5 nM, respectively (Table 1). None of the 3 ligands competed with binding of the $\text{A}\beta$ radioligand ^3H -florbetapir to plaque-rich AD cortical tissue sections. Figure 2 shows representative inhibition curves for RO6958948 using ^3H -T808 or ^3H -florbetapir binding to NFT-rich AD cortical tissue sections.

The specificity of RO6958948, RO6931643, and RO6924963 for tau aggregates in NFTs was demonstrated by in vitro autoradiographic analysis of the tritiated versions of all 3 compounds. In AD Braak V temporal cortex sections, all 3 radioligands showed an autoradiographic binding pattern comparable to that of the tau-specific radioligand ^3H -T808 (Fig. 3). The typical layered binding pattern agreed with different densities of NFTs and neuropil threads in various layers of cortical AD tissue. Autoradiographic binding of all 3 tracer candidates was characterized by favorable signal-to-noise ratios reflected by low nonspecific binding to white matter and gray matter in NFT-free tissue sections from healthy controls (Table 1). Low nonspecific binding and absence of a distinct binding pattern in NFT-free temporal cortex tissue from healthy controls excluded significant high-affinity binding to other central nervous system targets and thus supported the specificity of all 3 radiotracer candidates for tau aggregates. This finding was confirmed by a Cerep selectivity screen against a panel of representative central nervous system targets (Supplemental Table 1; supplemental materials are available at <http://jnm.snmjournals.org>).

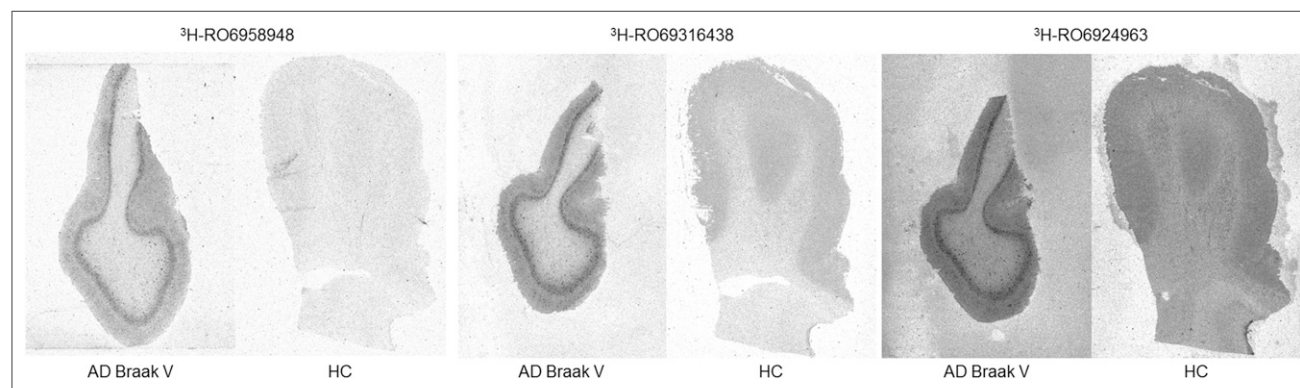


FIGURE 3. In vitro autoradiography of ^3H -RO6958948, ^3H -RO6931643, and ^3H -RO6924963 using cortical tissue sections from AD tissue donor and healthy control (HC).

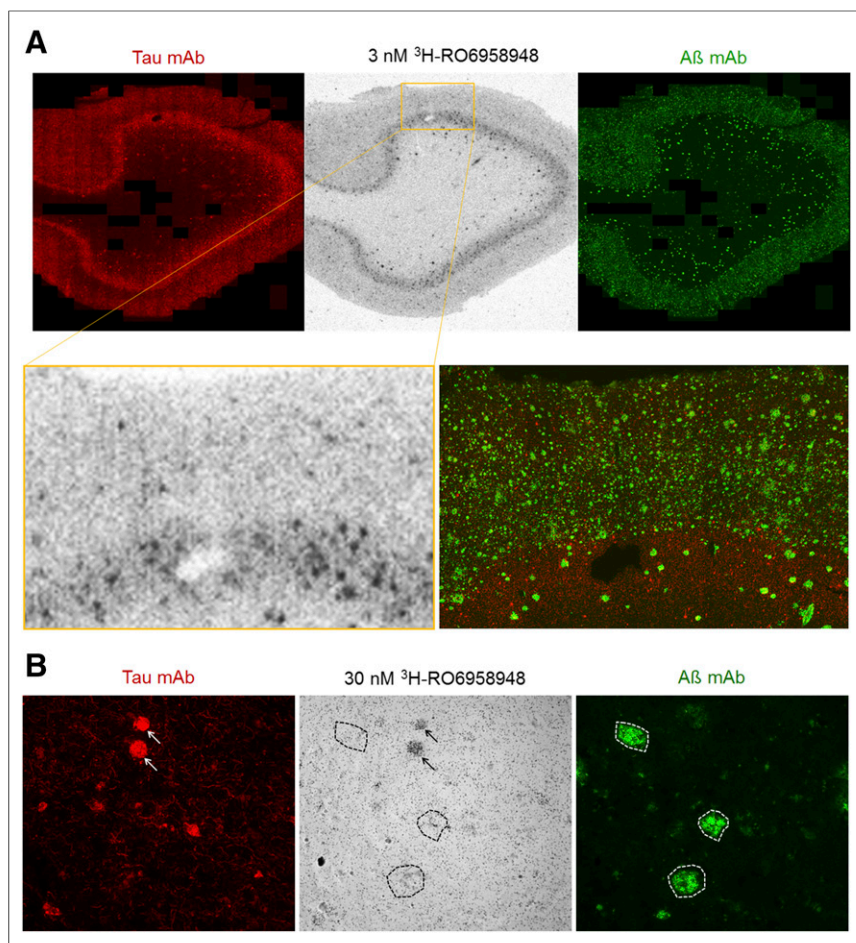


FIGURE 4. (A) Macroscopic colocalization of autoradiographic ^3H -RO6958948 binding with tau mAb and A β mAb staining on same cortex section from AD brain donor. At bottom is zoomed detail of autoradiogram, with immunohistochemical image (both tau mAb and A β mAb staining) on right. (B) Microscopic colocalization of ^3H -RO6958948 binding with tau mAb and A β mAb staining on same tissue section. Arrows show colocalization of radioligand binding (i.e., silver grain deposits) and tau mAb staining, and dashed circles show absence of silver grain deposits in areas of A β mAb staining.

Selectivity of all 3 tracer candidates for tau aggregates over A β plaques was further suggested by detailed colocalization studies of radioligand binding and antibody staining of tau aggregates. On the macroscopic level, the layered radioligand binding pattern compared favorably with antibody staining of tau aggregates on the same tissue section whereas the distribution pattern of A β antibody staining showed a different pattern (Fig. 4A, top). At higher magnification, colocalization of radioligand binding and tau mAb staining was even more evident (Fig. 4A, bottom), suggesting that hot spots in autoradiograms correspond to NFT binding whereas diffuse radioligand signal relates to binding to neuropil threads. This finding was corroborated by nuclear emulsion autoradiography (microautoradiography). Silver grain deposition favorably colocalized with tau mAb staining, whereas no accumulation of silver grains was found at sites of A β plaques staining with BAP-2a antibody (Fig. 4B). The selectivity of all 3 tracer candidates for tau aggregates over A β plaques was also supported by a quantitative correlation of radioligand binding intensity with signal sizes of immunohistochemical staining. Using 16 cortical AD tissue blocks from various Braak stages, binding levels increased with rising Braak stage (Fig. 5A). Radioligand

binding correlated well with pS422 tau mAb staining but not with BAP-2 A β mAb staining (Fig. 5B). The selectivity of tracer binding was further analyzed by displacement studies using 10 μM T808 for blockade. In the inferior temporal cortex, ^3H -RO6958948 showed strong binding that was displaced by more than 80% (Fig. 6). In contrast, in cerebellum and pons from AD Braak V patients, brain regions devoid of tau aggregates, there was negligible binding that was not displaced by 10 μM T808. Hippocampal binding in AD was specific since it was strongly displaced by high concentrations of T808, but binding levels in the hippocampus were lower than that observed in the adjacent parahippocampal gyrus and entorhinal cortex (Fig. 6B).

None of the 3 radioligands demonstrated any tau-related specific binding in tissue specimens from non-AD tauopathy tissue donors. Tau pathology with a heterogeneous distribution pattern was confirmed in tissue samples from progressive supranuclear palsy, corticobasal degeneration, and Pick disease donors by AT8 staining. However, radioligand binding was homogeneous, weak, and nondisplaceable (Supplemental Fig. 1).

RO6958948, RO6931643, and RO6924963 were successfully radiolabeled with either ^{18}F or ^{11}C . ^{18}F -RO6958948 was synthesized by nucleophilic displacement of the nitro group on an appropriate precursor, followed by purification using high-performance liquid chromatography. ^{18}F -RO6958948 was isolated with high radiochemical purity (100%) and high specific activity (1,550 GBq/ μmol) and in good radiochemical yield. RO6931643 and RO6924963 were synthesized by *O*- and *N*-methylation of their respective precursors

with ^{11}C -methyl iodide, followed by high-performance liquid chromatography purification. Both radiotracers were isolated with high radiochemical purity (>96%), high specific activity (>500 GBq/ μmol), and good radiochemical yields.

PET studies in tau-naïve baboons revealed favorable pharmacokinetic properties for all 3 tracer candidates, showing sufficient blood-to-brain clearance, with peak SUVs of 1.2–2.0 immediately after tracer injection and scan initiation (Table 2; Fig. 7). Sufficient penetration through the blood–brain barrier was also apparent from favorable K_1 values ranging from 0.10 to 0.70 min/min/mL. Radioactivity cleared rapidly from the baboon brain for the tracer candidates ^{18}F -RO6958948 and ^{11}C -RO6931643, with an SUV of less than 0.5 at 60 min after injection (Fig. 7). Brain washout of radioactivity was slower for ^{11}C -RO6924963. As expected, the distribution of radioactivity was homogeneous across all brain regions, because tau pathology was not present in the baboon brain. Some regional heterogeneity of tracer uptake was found only for ^{11}C -RO6924963, for which slightly higher radioactivity concentrations were identified in the putamen and thalamus. The observed low SUVs of ^{18}F -RO6958948 at later time points (e.g., after 60 min) and no or very low

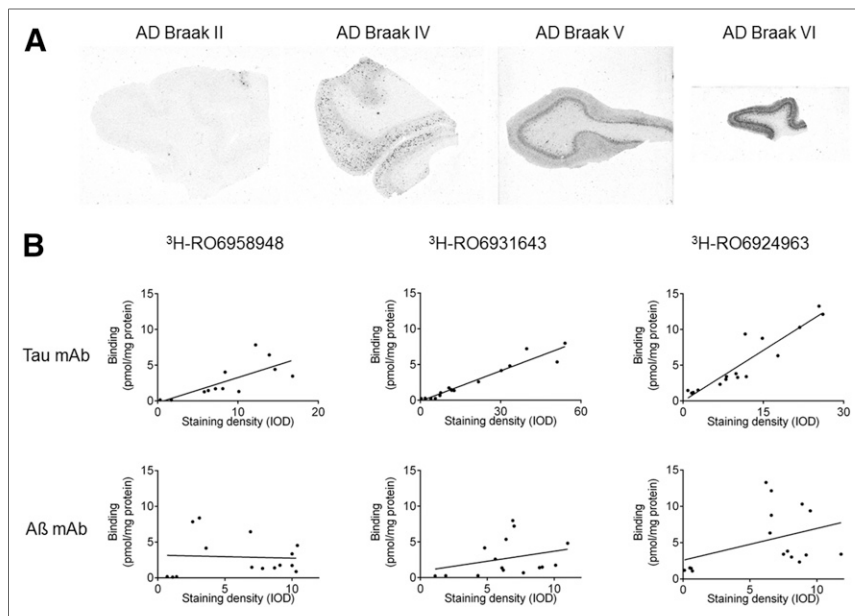


FIGURE 5. (A) Autoradiography of ^3H -RO6958948 in AD cortical tissue from various Braak stages. (B) Correlation of autoradiographic radioligand binding and tau mAb and A β mAb staining density on same tissue sections. IOD = integrated optical density.

regional variations strongly suggested low nonspecific retention and lack of off-target binding of this radioligand, whereas the time-activity curves for ^{18}F -T807 showed some regional heterogeneity and a slower decline (Supplemental Fig. 2). All radiotracer candidates were characterized by rapid and extensive metabolism (Supplemental Table 2). After about 10 min after injection, approximately 90% of plasma radioactivity was related to radiometabolites for the tracer candidate ^{11}C -RO6924963, whereas the rate of tracer metabolism was lower for ^{18}F -RO6958948 and ^{11}C -RO6931643. The kinetics of the 3 radioligands were better described with a 2-tissue compartmental model than with a 1-tissue model (i.e., Akaike information criterion values were lower in all regions for the 3 radioligands).

Plots of the plasma reference graphical analysis approached asymptotes by 20 min (coefficients of determination, R^2 of linear regression > 0.97 in all regions). Thus, the start of asymptote was set at 20 min for all radioligands. ^{18}F -RO6958948 showed lower regional variations in total distribution volume (coefficient of variation, 6.7%) than ^{11}C -RO6931643 (9.1%) or ^{11}C -RO6924963 (9.6%).

DISCUSSION

Previous efforts to develop PET tracers for tau aggregates of the AD type revealed limited significance and predictability for screening assays based on artificial tau fibrils or animal models of tauopathies. We therefore screened potential candidates for their binding affinity toward tau aggregates in tissue sections from AD cortex (20), which had been shown by immunohistochemistry (AT8, pS422) to have high NFT pathology. Such cortical AD brain tissue typically also contains high levels

of A β plaques. It is therefore crucial to use a tau-specific radioligand as a screening tool. T808 has been shown to be a selective, high-affinity NFT ligand but was not further developed because of in vivo defluorination (20). RO6958948, RO6931643, and RO6924963 were identified in an autoradiographic screening procedure as high-affinity displacers at the ^3H -T808 binding site on tau aggregates in native brain tissue sections from AD temporal cortex. The displacement curves in Figure 2 exemplify the high affinity of RO6958948 for the T808 binding site on tau aggregates and the lack of affinity for the florbetapir binding site on A β plaques, resulting in a tau-to-A β selectivity ratio of more than 500. The high selectivity of all 3 tracer candidates for tau aggregates over A β plaques was further demonstrated by

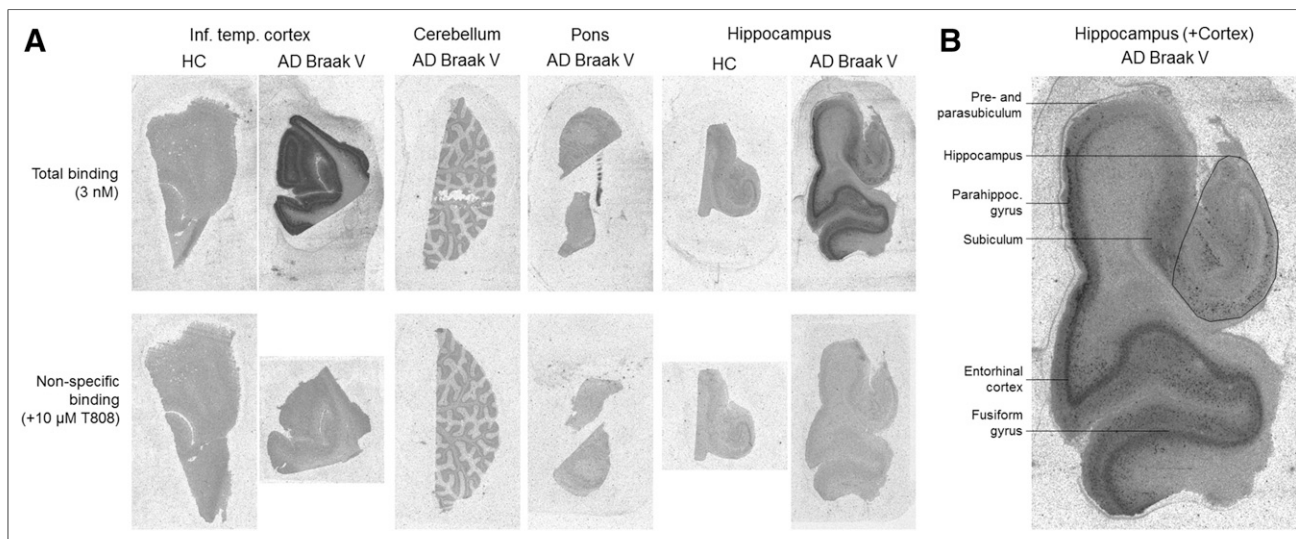


FIGURE 6. (A) Comparison of total binding and nonspecific binding of ^3H -RO6958948 (3 nM) determined by in vitro autoradiography in cortex, cerebellum, pons, and hippocampus tissue sections from healthy control (HC) and AD tissue donor. (B) Magnified autoradiogram showing hippocampus and adjacent cortical regions of AD Braak V tissue donor.

TABLE 2
Key In Vivo Parameters

Parameter	^{18}F -RO6958948	^{11}C -RO6931643	^{11}C -RO6924963
SUV_{peak}	2.0	1.2	1.9
K_1 (mL/mL/min)	0.70 ± 0.20	0.10 ± 0.01	0.49 ± 0.06
Ratio SUV_{peak} vs. SUV at 60 min after injection	11.8 ± 4.3	3.3 ± 0.4	1.8 ± 0.1
V_T (mL/mL)	6.4 ± 0.4	0.7 ± 0.1	29.1 ± 2.8

V_T = total distribution volume.

macroscopic and microscopic radioligand binding patterns that were comparable to that of tau mAb staining whereas the distribution pattern of A β mAb staining clearly showed different patterns (Fig. 4). In particular, nuclear emulsion autoradiography (microautoradiography) revealed no accumulation of silver grains at sites of A β plaques staining with BAP-2a antibody (Fig. 4B). In addition, quantitative correlation of radioligand binding intensity with the signal intensity of immunohistochemical staining was found only for pS422 tau mAb staining, not for BAP-2 A β mAb staining (Fig. 5).

The specificity of all 3 radioligands for tau aggregates and the lack of any significant off-target binding in vitro were demonstrated by autoradiography and displacement studies using the structurally dissimilar T808 and the authentic reference compounds. Consistent with a high selectivity for binding to NFTs, autoradiography in NFT-rich AD brain slices indicated that blockade of tracer binding was similar using either T808 or self-blocking. In addition, the level of nondisplaceable binding in NFT-rich AD brain slices was comparable to the total binding level in NFT-free cortical brain tissue from healthy controls. The absence of displaceable binding in NFT-free cortical brain tissue excluded significant radioligand binding to other cortical targets. In line with this finding, very low nonspecific binding was

observed in AD brain regions devoid of tau aggregates, such as cerebellum and pons (Fig. 6A), suggesting that both brain regions are suitable reference regions for quantitative analysis of PET data. Furthermore, Cerep profiling of all 3 candidates did not reveal significant binding to any other central nervous system target (Supplemental Table 1). Most notably, no affinity for MAO-A or MAO-B was found, as was recently observed for other tau PET tracer candidates (12,21). The absence of MAO-A and MAO-B off-target binding was also suggested for ^3H -RO6958948 in an autoradiographic displacement assay in which the MAO-A inhibitors clorgyline and RO0411049, as well as the MAO-B inhibitors L-deprenyl and lazabemide (10 μM each), did not affect radioligand binding in AD tissue sections (Supplemental Fig. 3). Altogether, these results provide clear evidence that the 3 tracer candidates have excellent selectivity for NFTs and lack any relevant in vitro off-target binding.

Our data from phosphor screen and nuclear emulsion autoradiography suggest that the bulk of the radioactive signal originates from radioligand binding to NFTs in AD brain sections. The hot spots in autoradiograms corresponded to binding to NFTs, whereas the diffuse radioligand signal corresponded to binding to neuropil threads in AD tissue samples, as exemplified for RO6958948 in Figure 4. In contrast, no ligand binding to tau aggregates in tissue sections from

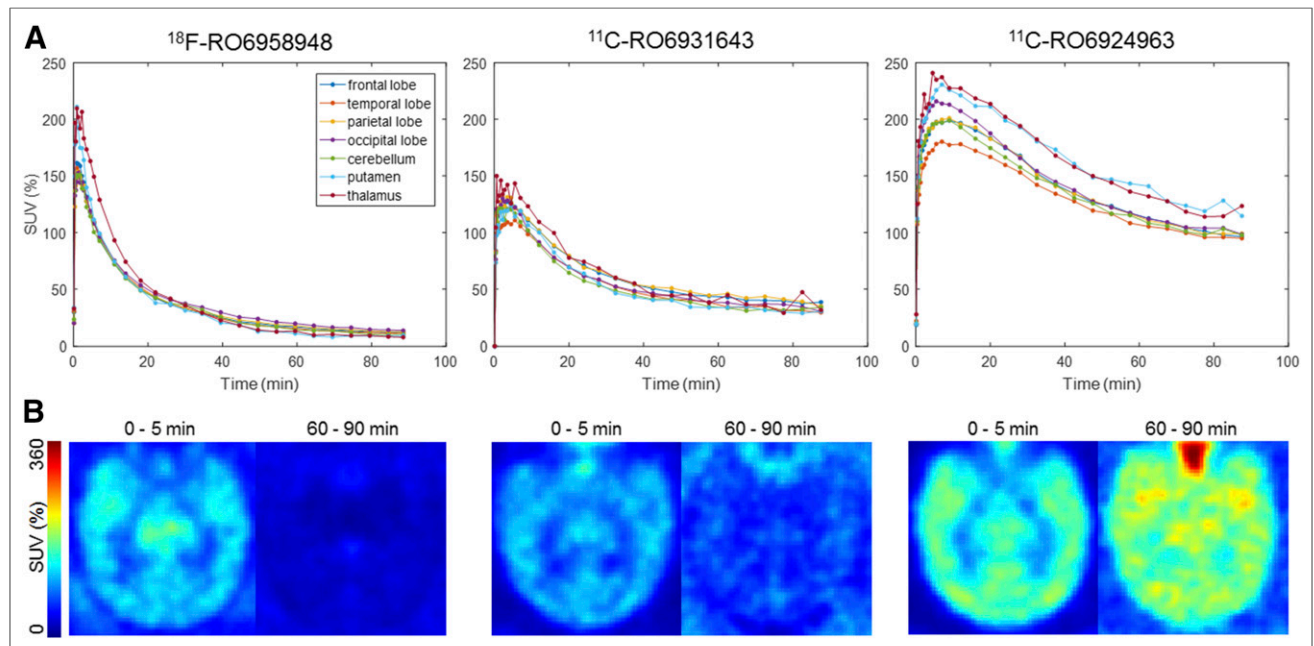


FIGURE 7. (A) Regional time-activity curves for ^{18}F -RO6958948, ^{11}C -RO6931643, and ^{11}C -RO6924963 from baboon PET images. (B) Averaged transaxial images of individual radioligands for earlier and later time points.

non-AD tauopathies such as progressive supranuclear palsy, corticobasal degeneration, and Pick disease was observed. This finding agrees with literature data for other tau tracers (9,10,22). It is hypothesized that all currently existing PET tracer candidates bind to tau aggregates in only a paired-helical filament conformation as present in AD brain tissue. In agreement with this hypothesis, none of our 3 tracer candidates displayed binding to tau aggregates in tissue from the tau transgenic mouse lines Tg4510 or Tau/PS2/APP (data not shown)—a finding that is also in accordance with published data for other tau tracer candidates.

All 3 tracer candidates showed strong blood-to-brain clearance in baboons, with favorably fast clearance from plasma and brain. As expected for NFT-naïve nonhuman primates, radioactivity uptake was homogeneously distributed in the brain. No increased uptake in white matter regions was observed, as is in line with the moderate lipophilicity of the 3 compounds. For all 3 tracer candidates, time-activity curves were declining until the end of the acquisition at 90 min after injection. In addition, radio-high-performance liquid chromatography analyses demonstrated the absence of radiometabolites more lipophilic than the parent compound. Both findings strongly suggest that brain-penetrant radiolabeled metabolites were not present at significant levels. Furthermore, no defluorination was observed for the tracer candidate ^{18}F -RO6958948. Direct comparison of the in vivo characteristics of all 3 tracer candidates in nonhuman primate PET experiments suggested that the candidate ^{18}F -RO6958948 is superior to ^{11}C -RO6931643 and ^{11}C -RO6924963, with higher peak SUVs and K_1 values, as well as better ratios of SUV_{peak} versus SUV at 60 min after injection. ^{18}F -RO6958948 also showed lower regional variations in total distribution volume, suggesting that ^{18}F -RO6958948 might be associated with the lowest regional variations in binding in this tau-free cohort.

CONCLUSION

^{18}F -RO6958948, ^{11}C -RO6931643, and ^{11}C -RO6924963 are promising PET tracers for visualization of tau aggregates in AD. All 3 ligands bind with nanomolar affinity and high specificity to tau aggregates, clearly lacking affinity for concomitant A β plaques in AD cortical tissue sections. The candidates also have favorable in vivo properties in tau-naïve baboons and thus possess favorable prerequisites for successful in vivo PET imaging of tau pathology in humans. A head-to-head comparison and detailed clinical validation of these 3 PET tracer candidates in patients with AD and healthy controls will be described in another report.

DISCLOSURE

This study was funded by a F. Hoffmann-La Roche Ltd. contract to the Johns Hopkins University (JHU). JHU faculty receive salary support through a number of sponsored research sources, including NIH grants S10-RR017219 and S10-RR023623 (both to Dean Wong). JHU faculty do not receive direct funding from Roche except via sponsored JHU contracts. No other potential conflict of interest relevant to this article was reported.

ACKNOWLEDGMENTS

We thank Patricia Glaentzlin, Céline Sutter, Svenja Moes, Jennifer Beck, Martin Edelmann, Christian Gut, Georg Etter, and Karina Mueller for excellent experimental support. Additionally, we thank the staff of the Johns Hopkins PET Center (Dr. Hayden T.

Ravert, Dr. William B. Mathews, Daniel P. Holt, and Andrew Hall) for their radiochemistry expertise. Special thanks go to Andrew Crabb and Dr. Arman Rahmim for reconstruction and physics support for the ECAT HRRT.

REFERENCES

1. Bierer LM, Hof PR, Purohit DP, et al. Neocortical neurofibrillary tangles correlate with dementia severity in Alzheimer's disease. *Arch Neurol.* 1995;52:81–88.
2. Nelson PT, Alafuzoff I, Bigio EH, et al. Correlation of Alzheimer disease neuropathologic changes with cognitive status: a review of the literature. *J Neuropathol Exp Neurol.* 2012;71:362–381.
3. Ariza M, Kolb HC, Moechars D, Rombouts F, Andrés JL. Tau positron emission tomography (PET) imaging: past, present, and future. *J Med Chem.* 2015;58:4365–4382.
4. Dani M, Brooks DJ, Edison P. Tau imaging in neurodegenerative diseases. *Eur J Nucl Med Mol Imaging.* 2016;43:1139–1150.
5. Shah M, Seibyl J, Cartier A, Bhatt R, Catafau AM. Molecular imaging insights into neurodegeneration: focus on α -synuclein radiotracers. *J Nucl Med.* 2014;55:1397–1400.
6. Chien DT, Bahri S, Szardenings AK, et al. Early clinical PET imaging results with the novel PHF-tau radioligand [F-18]-T807. *J Alzheimers Dis.* 2013;34:457–468.
7. Shcherbinin S, Schwarz AJ, Joshi A, et al. Kinetics of the tau PET tracer ^{18}F -AV-1451 (T807) in subjects with normal cognitive function, mild cognitive impairment, and Alzheimer disease. *J Nucl Med.* 2016;57:1535–1542.
8. Wooten DW, Guehl NJ, Verwer EE, et al. Pharmacokinetic evaluation of the tau PET radiotracer ^{18}F -T807 (^{18}F -AV-1451) in human subjects. *J Nucl Med.* 2017;58:484–491.
9. Lowe VJ, Curran G, Fang P, et al. An autoradiographic evaluation of AV-1451 tau PET in dementia. *Acta Neuropathol Commun.* 2016;4:58.
10. Marquie M, Normandin MD, Vanderburg CR, et al. Validating novel tau positron emission tomography tracer [F-18]-AV-1451 (T807) on postmortem brain tissue. *Ann Neurol.* 2015;78:787–800.
11. Maruyama M, Shimada H, Suhara T, et al. Imaging of tau pathology in a tauopathy mouse model and in Alzheimer patients compared to normal controls. *Neuron.* 2013;79:1094–1108.
12. Ng KP, Pascoal TA, Mathotaarachchi S, et al. Monoamine oxidase B inhibitor, selegiline, reduces ^{18}F -THK5351 uptake in the human brain. *Alzheimers Res Ther.* 2017;9:25.
13. Hostetler ED, Walji AM, Zeng Z, et al. Preclinical characterization of ^{18}F -MK-6240, a promising PET tracer for in vivo quantification of human neurofibrillary tangles. *J Nucl Med.* 2016;57:1599–1606.
14. Walji AM, Hostetler ED, Selnick H, et al. Discovery of 6-(fluoro- ^{18}F)-3-(1H-pyrrolo[2,3-c]pyridin-1-yl)isoquinolin-5-amine (^{18}F -MK-6240): a positron emission tomography (PET) imaging agent for quantification of neurofibrillary tangles (NFTs). *J Med Chem.* 2016;59:4778–4789.
15. Declercq LD, Rombouts F, Koole M, et al. Preclinical evaluation of ^{18}F -JNJ6439311, a novel PET tracer for tau imaging. *J Nucl Med.* 2017;58:975–981.
16. Gobbi L, Knust H, Koerner M, Muri D, inventors. F. Hoffmann-La Roche, assignee. Preparation of 2-phenylimidazo[1,2-a]pyrimidines as imaging agents for diagnosis of Alzheimer's disease. International patent WO2014187762A1. 2014.
17. Gobbi L, Knust H, Koerner M, Muri D, inventors. F. Hoffmann-La Roche, assignee. Preparation of diazacarbazole derivatives as tau PET ligands. International patent WO2015052105A1. 2015.
18. Rahmim A, Cheng JC, Blinder S, Camborde ML, Sossi V. Statistical dynamic image reconstruction in state-of-the-art high-resolution PET. *Phys Med Biol.* 2005;50:4887–4912.
19. Logan J, Fowler JS, Volkow ND, et al. Graphical analysis of reversible radioligand binding from time-activity measurements applied to [N- ^{11}C -methyl]-(-)-cocaine PET studies in human subjects. *J Cereb Blood Flow Metab.* 1990;10:740–747.
20. Zhang W, Arteaga J, Cashion DK, et al. A highly selective and specific PET tracer for imaging of tau pathologies. *J Alzheimers Dis.* 2012;31:601–612.
21. Vermeiren C, Mercier J, Viot D, et al. T807, a reported selective tau tracer, binds with nanomolar affinity to monoamine oxidase A [abstract]. *Alzheimers Dement.* 2015;11:283.
22. Sander K, Lashley T, Gami P, et al. Characterization of tau positron emission tomography tracer [^{18}F]AV-1451 binding to postmortem tissue in Alzheimer's disease, primary tauopathies, and other dementias. *Alzheimers Dement.* 2016;12:1116–1124.